Journal Pre-proofs

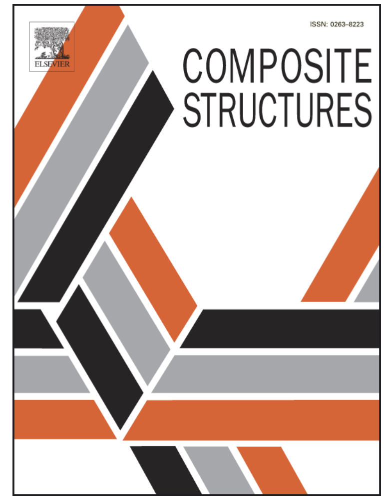

Shear behaviour of inorganic polymer concrete beams reinforced with basalt FRP bars and stirrups

Xiaochun Fan, Zhengrong Zhou, Wenlin Tu, Mingzhong Zhang

PII: S0263-8223(20)32827-0
DOI: https://doi.org/10.1016/j.compstruct.2020.112901
Reference: COST 112901

To appear in: *Composite Structures*

Received Date: 3 May 2020
Revised Date: 5 July 2020
Accepted Date: 26 August 2020

Please cite this article as: Fan, X., Zhou, Z., Tu, W., Zhang, M., Shear behaviour of inorganic polymer concrete beams reinforced with basalt FRP bars and stirrups, *Composite Structures* (2020), doi: https://doi.org/10.1016/j.compstruct.2020.112901

Shear behaviour of inorganic polymer concrete beams reinforced with basalt FRP bars and stirrups

Xiaochun Fan [a], Zhengrong Zhou [a], Wenlin Tu [b], Mingzhong Zhang [b,*]

[a] School of Civil Engineering and Architecture, Wuhan University of Technology, Wuhan 430070, China

[b] Department of Civil, Environmental and Geomatic Engineering, University College London, London WC1E 6BT, UK

Abstract: Inorganic polymer concrete (IPC) reinforced with basalt fibre reinforced polymer (BFRP) was proposed as a promising substitute of conventional reinforced concrete for structures to enhance their sustainability and durability. This paper, for the first time, presents a systematic study, experimental, theoretical and numerical, of shear behaviour of IPC beams reinforced with BFRP bars and stirrups considering the effects of stirrup spacing (S = 80, 100 and 150 mm) and shear span-to-depth ratio (λ = 1.5, 2.0 and 2.5). Result indicates that all BFRP-IPC beams fail in shear as a result of BFRP stirrup rupture and shear-compression failure. Compared to S, λ has a more pronounced influence on shear performance of BFRP reinforced IPC beams, with a maximum reduction of ultimate shear load by 29.4%. The simulation results show good agreement with experimental data, while the theoretical predictions according to existing design provisions for FRP reinforced concrete have a discrepancy of more than 30% with experiments due to lack of consideration of λ. Modified equations taking into account the effect of λ were then derived and used to predict the shear capacity of BFRP reinforced IPC beams, which agrees well with experimental data with an average discrepancy of only around 5%.

keywords: Geopolymer concrete; FRP; Shear capacity; Theoretical predictions; Finite element analysis

* Corresponding author. E-mail address: mingzhong.zhang@ucl.ac.uk (M. Zhang)

23 **Nomenclature**

A_f	Total cross-sectional area of longitudinal tension reinforcement (mm^2)	n_f	Ratio of modulus of elasticity of reinforcing bars to modulus of elasticity of concrete
A_{fv}	Total cross-sectional area of spiral reinforcement (mm^2)	r_b	Internal bend radius of the FRP spirals (mm)
d	Effective depth of tensile reinforcement (mm)	S	Spacing of spirals (mm)
d_b	Bar diameter (mm)	V_c	Shear strength of concrete (kN)
d_v	Effective shear depth (mm)	V_{cf}	FRP concrete shear strength (kN)
E_c	Modulus of elasticity of concrete (MPa)	V_{cr}	First diagonal shear crack (kN)
E_f	Modulus of elasticity of FRP reinforcing bars (MPa)	V_{exp}	Experimental shear strength (kN)
E_{fv}	Modulus of elasticity of FRP spirals (MPa)	V_f	Shear strength of stirrups
E_s	Modulus of elasticity of steel reinforcing bars (MPa)	V_p	Predicted shear strength from the previsions
f'_c	Specified compressive strength of concrete (MPa)	V_s	Simulated shear strength
f_{cr}	Cracking strength of concrete (MPa)	γ_b	Safety factor
f_{cu}	Compressive stress in struts (MPa)	α	Coefficient reflecting the influence of λ
f_{fu}	Tensile strength of straight portion of spirals (MPa)	ε_o	IPC strain at the maximum stress
f_{fv}	Stress in FRP spirals (MPa)	ε_{cu}	Strain at the failure stress
f'_{mcd}	Design compressive strength of concrete allowing for size effect (MPa)	ε_s	BFRP strain
M_d	Design bending moment ($N \cdot mm$)	θ	Angle of inclination of the principle diagonal compressive stress (in degrees)
M_f	Factored moment ($N \cdot mm$)	λ	Shear span-to-depth ratio
N_f	Factored axial force (kN)	ρ_f	FRP longitudinal reinforcement ratio

24

1. Introduction

Concrete is the most commonly used construction material in the world. The sustainability issue of the manufacture of concrete has been raised, concerning the production of Poland cement as the main component of raw materials, which accounts for around 7% of global CO_2 emissions [1]. In recent years, inorganic polymers, also called geopolymers, which are produced through the reaction of aluminosilicate source materials such as fly ash (FA) and ground granulated blast-furnace slag (GGBS) with alkaline activators, have attracted considerable attention [2]. Inorganic polymer concrete (IPC) is regarded as an innovative cement-free alternative to conventional Poland cement concrete (PCC) in the construction industry [3-5]. It is reported that IPC possesses comparable mechanical properties to PCC and superior resistance to corrosion, chemical attack, freeze-thaw cycles and fire with up to 80% less embodied energy and carbon footprint compared to PCC [6-9].

Corrosion of steel reinforcement is the main cause of deterioration of reinforced concrete (RC) structures. Many approaches have been proposed to mitigate the steel corrosion and improve the durability of RC structures, including the use of fibre reinforced polymer (FRP) bars as a substitute for internal steel reinforcement, which has recently emerged as an advance solution to the corrosion problem in RC structures [10, 11]. The most widely used FRP reinforcement in the construction industry is made from glass (GFRP), carbon (CFRP) and aramid (AFRP), among which GFRP and AFRP are sensitive to the alkaline environment within concrete due to the poor alkali resistance of fibres [12], while CFRP is still far too expensive for normal RC structures [2, 13]. More recently, basalt fibre reinforced polymer (BFRP) bars have been introduced to provide an alternative type of reinforcing material [14-16], which has a relatively lower cost with high accessibility and excellent resistance to acids, corrosion, high temperature, freeze-thaw cycles, vibration and impact loading [2, 17-20]. In addition, when under alkaline conditions, BFRP was found to perform better than GFRP and AFRP [21]. Therefore, BFRP has been considered as a promising substitution to conventional FRP reinforcing bars.

In the last few years, an increasing number of experimental efforts have been made to explore the mechanical behaviour of IPC elements reinforced with steel or conventional FRP bars and PCC elements reinforced with BFRP bars. In terms of the interactions between reinforcement and IPC, Castel and Foster [22] experimentally investigated the bond strength between steel bars and FA-based IPC, which was found to be 10% higher compared to steel reinforced PCC, while both specimens had a similar level of chemical adhesion on the steel surface. Moreover, it was reported that the bond strength of steel reinforced IPC after heat curing of 2 d was close to that of steel reinforced PCC after heat curing of 28 d, indicating the suitability of IPC for precast applications [22]. IPC was also observed to have a similar or higher bond strength than the equivalent PCC system in other studies [23-25], which was attributed to the higher splitting tensile strength of IPC compared to PCC [26]. With respect to BFRP reinforced concrete, the experimental studies on flexural and shear performance of concrete beams reinforced with BFRP bars indicated that BFRP reinforced concrete beams have a higher tensile strength than steel reinforced concrete beams, whereas the bond strength between the reinforcement and concrete is similar for both specimens [27, 28]. The shear capacity of general FRP reinforced concrete beam was found to be lower than that of steel reinforced concrete beam due to the lower axial stiffness of FRP reinforcement, which would cause an increase of diagonal cracks and thus impede the shear transfer through the aggregate interlock [29].

Considering the similar mechanical behaviour of steel reinforced IPC elements and BFRP reinforced normal concrete elements compared to conventional steel reinforced concrete elements, Fan and Zhang [2] recently proposed a new composite that combines IPC made of industrial by-products including FA and GGBS and BFRP bars to replace conventional steel reinforced concrete as a novel approach to improve the sustainability and durability of concrete infrastructure. A previous study [2] on the flexural behaviour of IPC beam reinforced with BFRP bars demonstrated that BFRP reinforced IPC beam and control steel reinforced concrete beam had similar development of cracking and crack patterns but different maximum crack width and load–displacement/strain response due to different mechanical performance of basalt and steel reinforcement. The mechanical behaviour of short IPC columns reinforced with BFRP bars under eccentric compression was investigated by Fan and Zhang [30], who observed that BFRP reinforced IPC columns had almost similar load–displacement/strain response up to final failure as the control steel reinforced concrete columns but an approximately 30% lower load carrying capacity than the control columns. Although the flexural behaviour and compressive behaviour of BFRP reinforced IPC beams and short columns respectively have been studied, to the best of the authors' knowledge, the shear behaviour of BFRP reinforced IPC has not been addressed. It is vital to extensively explore the shear performance of structural elements made of this novel sustainable and durable reinforced concrete to prove the feasibility of using it for concrete infrastructure.

To main purpose of this study is to provide a comprehensive understanding of the shear behaviour of IPC beams reinforced with BFRP bars and stirrups. IPC was made of blended FA and GGBS and alkaline activator and cured at ambient temperature. Four-point bending tests on BFRP reinforced IPC beams with various stirrup spacing (S = 80, 100 and 150 mm) and shear span-to-depth ratio (λ = 1.5, 2.0 and 2.5) were carried out to investigate the shear performance in terms of crack patterns, failure modes, load-deflection, load-strain response and shear capacity. Afterwards, finite element simulations and theoretical calculations as per design provisions for FRP reinforced concrete elements were undertaken to predict the shear capacity of BFRP reinforced IPC beams, which was compared with experimental results to validate numerical simulations and evaluate the applicability of existing design standards for BFRP reinforced IPC beams. Based on the analysis, the previsions were correspondingly modified to provide accurate predictions of shear performance and suitable design guidelines for BFRP reinforced IPC.

2. Experimental program

2.1. Materials

The IPC used in this study is a mixture of inorganic polymer binder, alkaline activator and fine and coarse aggregates. The inorganic polymer binder was a coalescence of low calcium (equivalent to ASTM class F) FA and class S95 GGBS with a mass ratio of 3:1. The chemical compositions of FA and GGBS are demonstrated in Table 1. The alkaline activator was prepared with solid sodium hydroxide (NaOH) and sodium silicate (Na_2SiO_3) solution, in which the NaOH powder was dissolved in water to obtain NaOH solution with a molarity of 10 M and the Na_2SiO_3 solution had a density of 1380 kg/m^3 and SiO_2/Na_2O ratio of 2.0. The alkaline activator-to-binder ratio was 0.4. The medium-sized river sand with a fineness modulus of 2.75 and apparent density of 2725 kg/m^3 was used as fine aggregate. The crushed stone with a particle size of 5-20 mm and apparent density of 2665 kg/m^3 was used as coarse aggregate. The modified polycarboxylate-based superplasticizer (SP) was applied as the admixture to adjust the workability of mixture. Table 2 shows the mix proportion of IPC used in this study, which was obtained based on the previous research [31].

The mixing procedure of IPC is presented in Fig. 1. Inorganic polymer binder along with fine and coarse aggregates were firstly dry mixed for 2 min to ensure homogeneous dispersion. Then, the alkaline solution and SPs were added to the mixture and mixed for another 4 min. The fresh concrete was cast into moulds with two different sizes including 150 mm cube and 150 × 300 mm cylinder after mixing. The specimens were de-moulded after 24 h and then placed in a standard curing room for moist curing of 27 d. After curing, the compressive and splitting tensile strength tests were carried out on the cubic specimens in accordance with GB/T 50081-2019 [32]. The axial compressive strength and elastic modulus tests on the cylindrical specimens were also conducted. Three samples were used for each test to determine variation and the average values were obtained, which indicated that the designed IPC had a compressive strength and splitting tensile strength of 31.3 MPa and 2.26 MPa, respectively and an elastic modulus of 25.8 GPa.

Deep threaded BFRP bars with diameters of 10 mm and 16 mm were used as longitudinal reinforcement, while the closed stirrups with a diameter of 8 mm were used as transverse reinforcement. Fig. 2 illustrates the BFRP longitudinal bars and stirrups used in this study. To determine the tensile strength and elastic modulus of BFRP bars, 5 BFRP bars with a length of 1300 mm were prepared and tested based on the procedure provided by GB/T 30022-2013 [33]. To avoid the damage caused by loading at the end of the bars, two steel tubes with a length of 400 mm were fixed at the two end anchorages of the tested bars by filling the tubes with two-component epoxy resin followed by curing of 5 d. The front view of the tested specimen with steel tubes is demonstrated in Fig. 3. After curing, the uniaxial tensile tests were carried out using a servo-hydraulic testing machine (LFV-10000kN).

Fig. 4 shows the BFRP bars at different testing stages. The measured bottom diameters of BFRP bars were used for the calculation of mechanical properties since the bottom cross-section of the specimen was less affected by the thread pulled out than the middle cross-section. Fig. 5 displays the stress-strain curves of 10-mm BFRP bars as an example. The corresponding mechanical properties of BFRP bars with diameters of 8, 10 and 16 mm are obtained and presented in Table 3. According to the results of uniaxial tensile tests, there was a linear stress-strain relationship in terms of the tensile behaviour of BFRP bars up to failure. The fracture of fibres can be observed starting from the surface of specimens when increasing the load until the rupture of the bars, as shown in Fig. 4b and c. The BFRP bars were abruptly destructed without any obvious yielding point. The measured tensile strength and elastic modulus of the 10 mm BFRP bars were 1275 MPa and 43.4 GPa, respectively. Compared to steel bars, BFRP bars are recognised as a reinforcement material with higher tensile strength, whereas the elastic modulus and ductility are relatively lower [14, 27, 30].

2.2. Specimen preparation

Fig. 6 illustrates the four-point bending test configuration and details of strain gauges on BFRP reinforcement and IPC. Five groups of IPC beams were prepared, and duplicate samples were tested for each of them (10 beams tested in total). The designed IPC beams were 120 mm in width and 200 mm in height, with a length of 2000 mm. The effective span and thickness of concrete cover were 1700 mm and 15 mm, respectively. All the beams consisted of four longitudinal BFRP bars, in which two 10-mm bars were placed on the top and the other two 16 mm bars were at the bottom of the specimen. The framework of the designed BFRP reinforcement is shown in Fig. 6b.

In this study, the emphasis was placed on the influences of two parameters, i.e. stirrup spacing (*S*) and shear span-to-depth ratio (λ) on the shear behaviour of BFRP reinforced IPC beams, where λ is defined as the ratio of shear span to the effective height of the beam section. Here, the effective height of the beam section was set as 169 mm. Details of the BFRP reinforced IPC beam specimens are given in Table 4. Each specimen was identified by a code starting with "SB". SB-1, SB-2 and SB-3 represent the specimens with a constant λ of 2.0 but various *S* of 80 mm, 100 mm and 150 mm respectively, which were used to investigate the influence of *S*. The specimens with a constant *S* of 100 mm but various λ of 1.5, 2.0 and 2.5, i.e. SB-4, SB-2 and SB-5 were prepared and tested to estimate the influence of λ.

2.3. Test setup and instrumentation

The load was applied to the specimens by means of a 50 t hydraulic machine in accordance with GB/T 50152-2012 [34]. A spreader beam supported by two steel plates was placed on top of the specimen, which is simply supported and loaded in the four-point bending setup as shown in Fig. 6. To monitor the evolution of strain on BFRP bars during loading, the strain gauges were attached to the middle of longitudinal bars and stirrups, as more shear stress would be experienced at the specified positions within the shear span, and the obtained average values of strain were used for analysis and comparison. For concrete, the strain gauges were placed on the side-surface of the specimen to determine the strain on concrete between two loading points. The deflections of the specimen at midspan and two ends of the specimen were monitored using linear variable differential transformers (LVDT). In addition, the crack patterns of the specimens at different loading stages were recorded.

3. Experimental results and discussion

This section presents the shear behaviour of the designed BFRP reinforced IPC beams obtained from experiments in terms of crack patterns, failure modes, load-deflection response, load-strain response and shear capacity, based on which the effects of S and λ on shear performance of the designed specimens are estimated and discussed in detail.

3.1. Crack patterns and failure modes

Figs. 7-10 demonstrate the crack patterns and failure modes of the tested beams. Similar crack patterns can be found from SB-1 to SB-5. The initial crack was observed in the constant bending moment zone (i.e. pure bending zone) at a load ranging from 16 kN to 20 kN for all specimens. The experimental results of first crack load for all specimens are summarised in Table 5. A comparison between SB-2, SB-4 and SB-5 was made to investigate the effect of λ. The increase of λ from 1.5 to 2.5 causes a reduction of the first crack load by 25%, which implies that the first crack is initiated at a higher load level for specimens with a lower λ. In comparison with SB-5, SB-4 experiences a less significant moment, which can be attributed to the decrease of shear span that results in a smaller moment arm and bending moment in the pure bending zone. Therefore, a higher first crack load can be achieved in SB-4. This agrees well with the previous experimental findings for BFRP reinforced concrete beams that the first crack initiates at a higher load for beams with a lower λ [29]. Nevertheless, S has no noticeable influence on the first crack load of BFRP reinforced IPC, which is about 18 kN for all three groups, i.e. SB-1, SB-2 and SB-3.

At the beginning, some flexural vertical cracks occur at the bottom of the beam aligning to the two loading points. The propagation of those vertical cracks is rapid and sudden with the energy released during crack growth. As the load increases, more vertical cracks are initiated within the constant bending moment region, which develop rapidly towards the neutral axis and concrete compression zone. The flexural-shear cracks, also known as the inclined cracks, are formed in the shear-span area of the beam and develop towards both loading and supporting points. These inclined cracks can be observed in all specimens (see Figs. 7 and 9). As further load is applied, the width of both vertical cracks in the pure bending zone and the inclined cracks in the shear-span area increases, while the inclined cracks have a higher increment in width than vertical cracks. To a certain loading level, the inclined cracks in the shear-span area propagate through the beam with the rupture of the stirrups, as illustrated in Figs. 9 and 11.

According to the results, the failure modes of the tested BFRP reinforced IPC beams are close to the shear-compression failure, which is defined by the rupture of stirrups and crushing of concrete near the loading points (see Figs. 8 and 10). This is consistent with the previous study [29] that the BFRP reinforced concrete beams experienced shear-compression failure when λ was no more than 2.5, but experienced tension failure when λ was between 2.5 and 3.5.

3.2. Load-deflection response at midspan

Fig. 11 shows the load-deflection response at midspan. A summary of midspan deflection for all specimens is given in Table 5. It can be observed that the BFRP reinforced IPC beams exhibit a bilinear load-deflection behaviour. The curves can be divided into two regions, which stand for the loading stages before and after the occurrence of cracks. Initially, the linear segment is steep and almost identical for all beams prior to the flexural cracking. The flexure stiffness is nearly the same for all the specimens before cracking occurs, due to the contribution of the moment of inertia in the IPC section [35]. The second linear segment represents the cracking response with a decreased stiffness and increased deflection up to failure, which is experienced by all the specimens in the IPC section. This indicates that the moment of inertia in the IPC section is reduced due to the successive flexural and shear cracking. Therefore, the contribution of BFRP reinforcement tends to be more significant when the cracks initiate and propagate towards the neutral axis. Moreover, the second segment is linear until the failure load is achieved, which can be ascribed to the linear elastic properties of BFRP reinforcement, as shown in Fig. 5 [36].

As seen in Fig. 11a, the overall loading-deflection response is relatively independent on S, with nearly the same tendency from SB-1 to SB-3, which means the change of S has a limited effect on the stiffness of BFRP reinforced IPC beam. Comparing SB-1 with SB-3, the midspan deflection is decreased by 17.7%, which can be ascribed to the less contribution of stirrups to the bending moment as S increases from 80 to 150 mm. However, λ has a more significant influence on the load-deflection curves when S is kept constant in specimens SB-2, SB-4 and SB-5, as shown in Fig. 11b. It is depicted that as λ is increased from 1.5 to 2.5 with a constant S, the overall stiffness of BFRP reinforced IPC beam is reduced by approximately 42.6%. This implies that the increase of λ can cause a less rigid body to carry the load. Furthermore, the midspan deflection is increased by about 25.1% with the increase of λ from 1.5 (SB-4) to 2.5 (SB-5), which can be attributed to the increase of bending moment that leads to a subsequent increase of deflection of the beam.

3.3. Load-strain response of inorganic polymer concrete

Fig. 12 shows the load-strain response of IPC with various values of *S* and *λ*. The corresponding shear, compressive and tensile strain are labelled as SB-1-S, SB-1-C, and SB-1-T, respectively. All the specimens have similar load-strain response in the IPC section. At the early stage of loading, the strain is very small due to the collaboration of IPC and BFRP reinforcement to carry the load and large initial stiffness of the BFRP reinforced IPC beams. In this stage, the changes of *S* and λ have a slight influence on the strain. As the load increases, the slope of the load-strain curve has a sharp change, implying that the initial cracking load is achieved. The strain then increases gradually with a less significant gradient as the load increases. Comparing the specimens with different *S* (Fig. 12a), the increase of *S* from 80 mm to 150 mm results in a steeper slope of the strain curves with an increase of the beam stiffness by about 73%, which can be explained by the fact that the interaction between IPC and BFRP reinforcement for load bearing capacity is enhanced with the decrease of *S*. Subsequently, the deformation is reduced. Additionally, under the same applied load, the slope of the load-strain curve is reduced significantly with the strain increased from about 500 με to 3000 με when increasing λ from 1.5 to 2.5 (Fig. 12b). This suggests that a larger deformation is achieved when λ of the specimen is increased, resulting in a smaller stiffness, which can be explained by the fact that the increase of λ can lead to an increasing amount of reinforcement within the shear-span area, which contributes to a declined stiffness in the IPC section.

As the load increases, the shear cracks initiate and propagate with rapid increase in crack width, which results in a significant increase of strain, followed by the failure of strain gauges. It can be observed from Fig. 12 that there is a sudden jump of the strain towards the end of the load-strain curve corresponding to the deformation after failure. In addition, the obtained load-strain response is consistent with the previous results of failure mode and crack patterns that the increase of λ can negatively affect the shear behaviour of BFRP reinforced IPC beams in terms of first crack load and ultimate shear load, which are decreased by 20% and 29.4%, respectively with increasing λ from 1.5 (SB-4) to 2.5 (SB-5), as seen in Table 5.

3.4. Load-strain response of BFRP longitudinal bars and stirrups

Fig. 13 shows the load-strain response of BFRP longitudinal bars. Before cracking, BFRP bars have similar unremarkable strain with the IPC section. The slope of the load-strain curve becomes gradually steadier when the applied load exceeds the first crack load. The increase of *S* results in a slight increase of the strain of longitudinal bars (see Fig. 13a). When the load reaches 80 kN, the strain is increased by approximately 9.5% with increasing S from 80 mm (SB-1) to 150 mm (SB-3), which reveals that S has an insignificant influence on the load-strain response of BFRP longitudinal bars. This result is consistent with the load-deflection curves shown in Fig. 11, which can be ascribed to the force transferred from IPC to longitudinal bars after cracking, whereas the stirrups as transverse reinforcement contribute less conspicuously to carry longitudinal force. However, with respect to λ, there is a more prominent effect on the load-strain response compared to S. As seen in Fig. 13b, the strain is increased by around 57.1% when λ increases from 1.5 (SB-4) to 2.5 (SB-5) at the loading of 80 kN. This agrees well with the findings shown in Fig. 12 that under the same load levels, the increase of λ can lead to an increase of strain in both IPC section and BFRP reinforcement.

Fig. 14 illustrates the load-strain response of the BFRP stirrups at different locations between the loading point and end of the beam, which can be divided into two linear stages. In the beginning, the strain of stirrups for all the specimens is lower than 100 με and increases slowly with the applied load. Once the cracks are initiated and propagate to reach the stirrups, the strain of stirrups has a sudden increase towards 3000 με when the applied load is close to the ultimate load. The increase of S results in the decreased number of stirrups to carry the load according to Fig. 14a. From SB-1 to SB-3, the number of stirrups that contributes to the shear capacity is reduced from 4 to 2 and thus the average strain of stirrups is decreased under the same load. Conversely, the increase of S and λ can result in an increase of the average strain of stirrups, which can be explained by the fact that more stirrups participate in carrying the applied load (Fig 14b).

3.5. Shear capacity

Fig. 15 shows the shear capacity of BFRP reinforced IPC beams against S and λ. The corresponding values are summarised in Table 5. There is a decreasing trend of the ultimate shear strength with the increase of both S and λ. The shear strength is reduced by 6.6% and 15% when S is increased from 80 mm to 100 mm and 150 mm, respectively. This is because the BFRP reinforcement with a smaller S can lead to an increasing number of stirrups that contributes to the shear resistance. Herein, the evolution of cracks can be restrained to a certain extent, while the IPC section after cracking can still bear the load. In addition, the BFRP stirrups together with the BFRP longitudinal bars act as hoops to restrict the concrete, which also helps increase the shear capacity of the tested specimens. On the other side, the ultimate shear strength is decreased by 3.9% and 29.4% when λ is increased from 1.5 to 2.0 and 2.5, respectively. As seen in Fig. 9, the increase of λ results in a decrease of the angle of critical shear cracks and therefore the load-bearing capacity of the corresponding IPC section is reduced as well as the shear capacity.

3.6. Comparison between experimental and predicted shear strength

The design previsions for shear behaviour of normal FRP reinforced concrete are adopted in this study. The ultimate shear strength of BFRP reinforced beams predicted using the previsions of ACI 440.1R-06 [37], CAN/CSA S802-12 [38], JSCE-97 [39] and GB50608-2010 [40] is compared with the experimental results. The corresponding equations for calculating the shear capacity are given in Appendix. It is worth noting that these equations are developed based on the experimental results of GFRP, CFRP and AFRP reinforced concrete beams [29]. To investigate the feasibility of using these shear design previsions for BFRP reinforced concrete beams, the predicted results are calculated and summarised in Table 6.

In these previsions, it is defined that the shear resistance (V) of a beam with stirrup bars consists of the contributions of stirrups (V_f) and concrete (V_c):

$$V = V_c + V_f \tag{1}$$

Based on the calculation of V_c and V_f, the predicted shear strength of the specimen (V_p) can be determined, which is presented together with the experimental shear strength (V_{exp}) in Table 6. In addition, V_{exp}/V_p is obtained to quantify the discrepancy between the theoretical predictions and experimental results. In general, for all the previsions, the shear capacity of specimens with higher λ can be better predicted compared to that with higher S. It can be observed that the predicted results of SB-5 are the closest values to 1, which is consistent with the previous study [29] that the predicted shear capacity of FRP reinforced concrete beams with higher λ is relatively close to the experimental results.

It is noted that almost all the values of V_{exp}/V_p are larger than 1, indicating that the predicted shear strength using these previsions is underestimated compared to the experimental results. Among all the previsions, JSCE-97 provides the most conservative predictions, with the highest average value of V_{exp}/V_p of 2.94 and the largest standard deviation of 0.39, which suggests that it might not be suitable for the prediction of shear performance of BFRP reinforced IPC beams. The average value of V_{exp}/V_p for CSA is the lowest (i.e. 1.3), demonstrating that it is the closest prediction to the experimental results.

4. Finite element simulations

According to the predicted results, the average values of V_{exp}/V_p range from 1.3 to 2.94, which implies a comparative discrepancy between V_{exp} and V_p of more than 30%. Here, the finite element simulations were performed to determine the shear capacity and evaluate the possibility of modifying and improving the above-mentioned previsions, and thus propose a modified equation for the shear capacity design of BFRP reinforced concrete beams. To simulate the shear behaviour of BFRP reinforced IPC beams accurately under four-point bending considering various S and λ, the IPC, BFRP longitudinal bars and BFRP stirrups should be properly modelled. The inputs including element types, mesh size, material properties of the IPC and BFRP reinforcement, and boundary and loading conditions were set up. The finite element analysis was carried out using ABAQUS, where the 3D 8-node linear iso-parametric element (C3D8) that is suitable for brittle materials was applied to model IPC, while the 3D 2-node linear displacement truss element (T3D2) was used to simulate BFRP reinforcement. According to the material properties of IPC, the concrete damage plasticity (CDP) model was chosen to simulate the concrete behaviour under loading. The multi-nonlinear isotropic stress-strain curve of concrete was adopted (see Fig. 16a), which can be described as follows:

$$\begin{cases} y = ax + (3-2a)x^2 + (a-2)x^3 & (0 \le x \le 1) \\ y = \frac{x}{b(x-1)^2 + x} & (x \ge 1) \end{cases} \tag{2}$$

where $x = \varepsilon/\varepsilon_0$, $y = \sigma/f_c$, ε_0 is the strain at ultimate load, and f_c is the ultimate load.

A linear elastic stress-strain relation (Fig. 16b) is applied for BFRP longitudinal bars and stirrups [2], which can be described as:

$$\begin{cases} \sigma = E_f \varepsilon & (\varepsilon \le \varepsilon_f) \\ \sigma = 0 & (\varepsilon > \varepsilon_f) \end{cases} \tag{3}$$

where E_f denotes the elastic modulus of BFRP reinforcement, and ε_f is its ultimate strain.

Rigid bearing blocks are located at the supporting and loading points to avoid non-convergence problems, and the binding constrain is applied between these blocks and the concrete elements. The load is applied in the middle of the relevant rigid bearing blocks. The BFRP reinforcing bars and stirrups are embedded in IPC. The finite element model of IPC beam reinforced with BFRP bars and stirrups is demonstrated in Fig. 17.

To verify the finite element model, the simulation results are compared with the experimental data in terms of the load-deflection curves, ultimate load, mid-span deflection at failure, crack evolution and failure pattern. Fig. 18 shows a comparison between the simulated concrete damage patterns and measured crack patterns (SB-2 is chosen as an example). It can be observed that the positions of two major cracks obtained from simulation and experiments are similar, while the evolution of multiple cracks detected from experiments is more prominently (Fig 18c). This indicates the damage of concrete obtained from the CDP model is in the shear-span area with the development of shear-compression cracks, which is in good agreement with the experimental results presented in Fig. 18b-c. The simulated and measured ultimate load (V_s and V_{exp}) are summarised in Table 6. It can be found that the V_{exp}/V_s is in the range of 0.83 to 0.99 with a discrepancy of less than 5% for all the specimens except SB-4, which suggests that the used finite element model can predict the shear capacity of BFRP reinforced IPC beams with high accuracy. Fig. 19 displays a comparison between the simulated and experimental load-deflection curves of BFRP reinforced IPC beams at midspan. Although the simulated midspan deflection at different loading stages is higher than the measured data, with a maximum discrepancy of approximately 20%, similar tendencies can be observed for both curves, which show two linear segments with a decreased gradient as the load increases.

5. Predictions of shear capacity using the modified equations

In order to provide a more accurate design guideline for BFRP reinforced IPC beams, the existing previsions for conventional FRP reinforced concrete beams can be further modified based on the simulation results. Here, the equations in GB 50608-2010 [40] were chosen for modification. The experimental results reveal that λ has a dominant influence on the shear resistance of BFRP reinforced IPC beams. However, according to the calculation (see Appendix), λ was not included in those equation, which means the influence of λ was not taken into account when considering the contribution of the IPC section to the shear resistance of the specimens. To address this drawback, a coefficient related to λ was introduced and incorporated into Eq. (38) to modify the shear strength of concrete, which can be expressed as follows:

$$V_c = 0.86\alpha f_t b_w k h_{of} \tag{4}$$

$$\alpha = \frac{1}{A\lambda + B} \tag{5}$$

where α represents the coefficient considering the influence of λ.

According to the previous comparison, the finite element model can effectively simulate the shear capacity of the designed specimens with λ ranging from 1.5 to 2.5. Here, to further investigate the influence of λ, a wider range of λ is considered. The specimens with a range of λ from 0.8 to 3.8 are numerically studied and the corresponding simulation results are reported in Table 7. The relationship between λ and α is plotted in Fig. 20. The slope of the curve is increased with the increase of λ, which can be observed from the three segments with linear fitting curves in Fig. 20. In accordance with these fitting lines, the coefficient α can be described as a function of λ below:

$$\begin{aligned} &\alpha = 1/(0.15\lambda - 0.05) && (\lambda \leq 2.0) \\ &\alpha = 1/(0.44\lambda - 0.63) && (2.0 < \lambda < 3.0) \\ &\alpha = 1/(0.63\lambda - 0.118) && (\lambda \geq 3.0) \end{aligned} \tag{6}$$

Then, the contribution of concrete to the overall shear resistance in Eq. (4) can be rewritten as:

$$\begin{aligned} &V_c = \frac{86}{15\lambda - 5} f_t b_w k h_{of} && (\lambda \leq 2.0) \\ &V_c = \frac{86}{44\lambda - 63} f_t b_w k h_{of} && (2.0 < \lambda < 3.0) \\ &V_c = \frac{86}{63\lambda - 118} f_t b_w k h_{of} && (\lambda \geq 3.0) \end{aligned} \tag{7}$$

Thus, according to Eqs. (1), (7) and (41), the shear resistance of the designed BFRP reinforced IPC beams can be determined as follows:

$$V = \frac{86}{15\lambda - 5} f_t b_w k h_{of} + \frac{A_{fv} f_{fv} h_{of}}{S} \qquad (\lambda \leq 2.0)$$

$$V = \frac{86}{44\lambda - 63} f_t b_w k h_{of} + \frac{A_{fv} f_{fv} h_{of}}{S} \qquad (2.0 < \lambda < 3.0) \qquad (8)$$

$$V = \frac{86}{63\lambda - 118} f_t b_w k h_{of} + \frac{A_{fv} f_{fv} h_{of}}{S} \qquad (\lambda \geq 3.0)$$

$$f_{fv} = min\{0.003E_f, \varphi_{bend} f_{fd}\} \qquad (9)$$

The final shear capacity calculated using the original GB 50608-2010 [40] and the modified equations are plotted together with the experimental results in Fig. 21. It can be observed that the calculated shear capacity after the modification is very close to the experimental results with an average ratio of 0.95. Comparing the predicted results using the equations without and with modification, the accuracy was increased by approximately 30%, which indicates that it is important to consider the effect of λ when predicting the shear performance of BFRP reinforced IPC beams. The accuracy of the predicted results is effectively improved using the modified GB 50608-2010 [40].

6. Conclusions

In this study, the shear behaviour of inorganic polymer concrete (IPC) beams reinforced with BFRP bars and stirrups was investigated considering the effects of stirrup spacing (*S*) and shear span-to-depth ratio (λ). A comparison between experimental data and finite element simulation results and predictions based on the theoretical previsions was carried out. The main conclusions can be drawn as follows:

- BFRP reinforced IPC beams demonstrate a shear-compression failure mode with the crush of concrete and rupture of stirrups at the shear-span area. The cracks propagate rapidly after the initiation due to the low elastic modulus of BFRP reinforcement.
- There exhibits a positive linear relationship between the applied load and the midspan deflection of the specimens. The increase of *S* from 80 mm to 150 mm has an almost negligible effect on the flexural stiffness of beams, whereas the increase of λ from 1.5 to 2.5 results in an approximately 42.6% decrease of the beam stiffness. This suggests that λ has a more pronounced effect on the load-deflection response of BFRP reinforced IPC beam specimens. Compared to *S*, λ shows a more significant influence on the ultimate load of the specimens, which is decreased by 29% with the increase of λ from 1.5 to 2.5.
- The load-strain response of BFRP reinforced IPC beams indicates that the increase of *S* leads to a decrease of strain while the relationship is inversed when increasing λ. Regarding the longitudinal BFRP bars, the increase of *S* and λ results in the growth of their strain by around 9.5% and 57.1%, respectively at the loading level of 80 kN. Moreover, the load-strain curve of stirrups shows that

fewer stirrups contribute to carrying the applied load when increasing *S*.

- The predicted results determined using the theoretical previsions and the finite element simulation results obtained using concrete damage plasticity model were compared with experimental data, which reveals that the simulation results are in good agreement with experimental data with discrepancies of less than 5%. The equations in GB 50608-2010 [40] were modified by incorporating a coefficient factor α related to λ and then used to predict the shear performance of BFRP reinforced IPC beams, which provides an approximately 30% more accurate predictions compared to the original equations. The theoretical predictions using the modified equations agree well with experimental data. BFRP reinforced IPC is a new composite as a promising alternative to conventional reinforced concrete for structural applications. It is vital to investigate the bond behaviour between IPC and BFRP reinforcement in order to gain a comprehensive understanding of the mechanical behaviour of BFRP reinforced IPC elements under different loading conditions. This is the subject of ongoing research, the results of which will be presented in future publications.

Acknowledgements

X. Fan gratefully acknowledges the financial support from the National Key Technology Support Program, China under Grant No. 2014BAB15B01. The financial support provided by the Engineering and Physical Sciences Research Council (EPSRC), UK under Grant Nos. EP/R041504/1 and 1836739 to M. Zhang is also gratefully acknowledged.

Appendix: shear design previsions

ACI 440.1R-06

According to ACI 440.1R-06, the shear strength of concrete can be calculated as follows:

$$V_c = \frac{2}{5}\sqrt{f'_c}b_w c \tag{10}$$

$$c = kd \tag{11}$$

$$k = \sqrt{2\rho_f n_f + (\rho_f n_f)^2} - \rho_f n_f \tag{12}$$

$$\rho_f = A_f / b_w d \tag{13}$$

$$n_f = \frac{E_f}{E_c} \tag{14}$$

where ρ_f is reinforcement ratio, and n_f is modular ratio.

As per ACI 440.1R-06, the shear strength of FRP stirrups can be calculated as follows:

$$V_f = \frac{A_{fv} f_{fv} d}{s} \tag{15}$$

$$f_{fv} = 0.004E_f \leq f_{fb} \tag{16}$$

$$f_{fb} = (0.05\frac{r_b}{d_b} + 0.3) f_{fu} \leq f_{fu} \tag{17}$$

CSA S806-12

According to CSA S806-12, the shear strength of concrete can be calculated as follows:

$$V_c = 0.05\lambda'\varphi_c k_m k_r k_a k_s (f'_c)^{\frac{1}{3}} b_w d_v \quad (18)$$

$$k_m = \sqrt{\frac{v_f d}{M_f}} \leq 1.0 \quad (19)$$

$$k_r = 1 + (E_f \rho_f)^{\frac{1}{3}} \quad (20)$$

$$1.0 \leq k_a = \frac{2.5}{\frac{M_f}{V_f d}} \leq 2.5 \quad (21)$$

$$k_s = \frac{750}{450 + d} \leq 1.0 \quad (22)$$

$$d_v = max\,(0.9d, 0.72h) \quad (23)$$

$$0.11\varphi_c \sqrt{f'_c} b_w d_v \leq V_c \leq 0.22\varphi_c \sqrt{f'_c} b_w d_v \quad (24)$$

The shear strength provided by stirrups can be calculated as follows:

$$V_f = \frac{0.4\varphi_f A_{fv} f_{fu} d_v}{s} cot\,\theta \quad (25)$$

$$\theta\ = 30^o + 7000\varepsilon_l \leq 60^o \quad (26)$$

$$f_{fu} \leq 0.005E_f \quad (27)$$

The strength of stirrups equals to $min\,(0.005E_f, 0.4f_{fu})$.

JSCE-97

According to JSCE-97, the shear strength of concrete can be obtained as follows:

$$V_c = \beta_d \cdot \beta_p \cdot \beta_n \cdot f_{vcd} \cdot b_w \cdot d/\gamma_b \quad (28)$$

$$f_{vcd} = 0.2\sqrt[3]{f'_{cd}} \leq 0.72MPa \quad (29)$$

$$\beta_d = \sqrt[4]{1/d} \leq 1.5 \quad (30)$$

$$\beta_p = \sqrt[3]{100\rho_f E_f/E_0} \leq 1.5 \quad (31)$$

$$\beta_n = 1.0 \text{ (no axial force)} \quad (32)$$

The shear strength of stirrups is determined by:

$$V_f = \left[A_{fv} E_{fv} \varepsilon_{fwd} \left(\frac{sin\alpha_s + cos\alpha_s)}{s}\right]z/\gamma_b \quad (33)$$

$$\varepsilon_{fwd} = \sqrt{f'_{mcd} \frac{\rho_w E_{fu}}{\rho_{web} E_w}} \left[1 + 2\left(\frac{\sigma'_N}{f'_{mcd}}\right)\right] \times 10^{-4} \leq f_{fbd}/E_w \quad (34)$$

$$f_{fbd} = (0.05\frac{r}{d_b} + 0.3) f_{fu}/\gamma_{mfb} \quad (35)$$

$$f'_{mcd} = \left(\frac{h}{300}\right)^{-1/10} \cdot f'_{cd} \quad (36)$$

$$\sigma'_N = (N'_d + P_{ed})/A_g \leq 0.4f'_{mcd} \quad (37)$$

GB 50608-2010

The shear strength of concrete can be calculated according to GB 50608-2010 as:

$$V_c = 0.86 f_t b_w k h_{of} \tag{38}$$

$$k = \sqrt{2\rho_f \alpha_f + (\rho_f \alpha_f)^2} - \rho_f \alpha_f \tag{39}$$

$$\rho_f = A_f / b_w h_{of} \tag{40}$$

The shear strength of stirrups can be calculated as follows:

$$V_f = \frac{A_{fv} f_{fv} h_{of}}{s} \tag{41}$$

$$A_{fv} = n A_{fv1} \tag{42}$$

$$f_{fv} = min\{0.004 E_f, \varphi_{bend} f_{fd}\} \tag{43}$$

$$\varphi_{bend} = (0.3 + 0.05 \frac{r_v}{d_v}) \tag{44}$$

References

[1] Juenger MCG, Siddique R. Recent advances in understanding the role of supplementary cementitious materials in concrete. Cement Concrete Research 2015;78:71-80.

[2] Fan X, Zhang M. Experimental study on flexural behaviour of inorganic polymer concrete beams reinforced with basalt rebar. Composites Part B: Engineering 2016;93:174-83.

[3] Mehta A, Siddique R. An overview of geopolymers derived from industrial by-products. Construction and Building Materials 2016;127:183-98.

[4] Yu R, Tang P, Spiesz P, Brouwers HJH. A study of multiple effects of nano-silica and hybrid fibres on the properties of Ultra-High Performance Fibre Reinforced Concrete (UHPFRC) incorporating waste bottom ash (WBA). Construction and Building Materials 2014;60:98-110.

[5] Tang P, Florea MVA, Spiesz P, Brouwers HJH. Application of thermally activated municipal solid waste incineration (MSWI) bottom ash fines as binder substitute. Cement Concrete Composites 2016;70:194-205.

[6] Sofi M, van Deventer JSJ, Mendis PA, Lukey GC. Engineering properties of inorganic polymer concretes (IPCs). Cement Concrete Research 2007;37(2):251-7.

[7] Hu S, Wang H, Zhang G, Ding Q. Bonding and abrasion resistance of geopolymeric repair material made with steel slag. Cement and Concrete Composites. 2008;30(3):239-44.

[8] Ma CK, Awang AZ, Omar W. Structural and material performance of geopolymer concrete: A review. Construction and Building Materials 2018;186:90-102.

[9] Mo KH, Alengaram UJ, Jumaat MZ. Structural performance of reinforced geopolymer concrete members: A review. Construction and Building Materials 2016;120:251-64.

[10] Poursaee A. Corrosion of steel in concrete structures. Corrosion of Steel in Concrete Structures: Elsevier; 2016. p. 19-33.

[11] Marcos-Meson V, Michel A, Solgaard A, Fischer G, Edvardsen C, Skovhus TL. Corrosion resistance of steel fibre reinforced concrete - A literature review. Cement Concrete Research 2018;103:1-20.

[12] Sim J, Park C, Moon DY. Characteristics of basalt fiber as a strengthening material for concrete structures. Composites Part B: Engineering 2005;36(6-7):504-12.

[13] Herwig A, Motavalli M. Axial behavior of square reinforced concrete columns strengthened with lightweight concrete elements and unbonded GFRP wrapping. Journal of Composites for Construction. 2012;16(6):747-52.

[14] Amran YHM, Alyousef R, Rashid RSM, Alabduljabbar H, Hung CC. Properties and applications of FRP in strengthening RC structures: A review. Structures. 2018;16:208-38.

[15] Schmidt JW, Bennitz A, Taljsten B, Goltermann P, Pedersen H. Mechanical anchorage of FRP tendons - A literature review. Construction and Building Materials 2012;32:110-21.

[16] Al-saadi AU, Aravinthan T, Lokuge W. Structural applications of fibre reinforced polymer (FRP) composite tubes: A review of columns members. Composite Structures 2018;204:513-24.

[17] Dhahir MK, Nadir W. A compression field based model to assess the shear strength of concrete beams reinforced with longitudinal FRP bars. Construction and Building Materials 2018;191:736-51.

[18] Wang ZK, Zhao XL, Xian GJ, Wu G, Raman RKS, Al-Saadi S. Durability study on interlaminar shear behaviour of basalt-, glass- and carbon-fibre reinforced polymer (B/G/CFRP) bars in seawater sea sand concrete environment. Construction and Building Materials 2017;156:985-1004.

[19] Ashour AF. Flexural and shear capacities of concrete beams reinforced with GFRP bars. Construction and Building Materials 2006;20(10):1005-15.

[20] Yang X, Gao WY, Dai JG, Lu ZD, Yu KQ. Flexural strengthening of RC beams with CFRP grid-reinforced ECC matrix. Composite Structures 2018;189:9-26.

[21] Lee JJ, Song J, Kim H. Chemical stability of basalt fiber in alkaline solution. Fibers and Polymers. 2014;15(11):2329-34.

[22] Castel A, Foster SJ. Bond strength between blended slag and Class F fly ash geopolymer concrete with steel reinforcement. Cement Concrete Research 2015;72:48-53.

[23] Songpiriyakij S, Pulngern T, Pungpremtrakul P, Jaturapitakkul C. Anchorage of steel bars in concrete by geopolymer paste. Materials & Design. 2011;32(5):3021-8.

[24] Sarker PK. Bond strength of reinforcing steel embedded in fly ash-based geopolymer concrete. Materials and Structures. 2011;44(5):1021-30.

[25] Menna C, Asprone D, Ferone C, Colangelo F, Balsamo A, Prota A, et al. Use of geopolymers for composite external reinforcement of RC members. Composites Part B: Engineering. 2013;45(1):1667-76.

[26] Nguyen KT, Ahn N, Le TA, Lee K. Theoretical and experimental study on mechanical properties and flexural strength of fly ash-geopolymer concrete. Construction and Building Materials 2016;106:65-77.

[27] Ge WJ, Zhang JW, Cao DF, Tu YM. Flexural behaviors of hybrid concrete beams reinforced with BFRP bars and steel bars. Construction and Building Materials 2015;87:28-37.

[28] Tomlinson D, Fam A. Performance of concrete beams reinforced with basalt FRP for flexure and shear. Journal of Composites for Construction. 2015;19(2):04014036.

[29] Issa MA, Ovitigala T, Ibrahim M. Shear behavior of basalt fiber reinforced concrete beams with and without basalt FRP stirrups. Journal of Composites for Construction. 2015;20(4):04015083.

[30] Fan X, Zhang M. Behaviour of inorganic polymer concrete columns reinforced with basalt FRP bars under eccentric compression: An experimental study. Composites Part B: Engineering 2016;104:44-56.

[31] Fang G, Ho WK, Tu W, Zhang M. Workability and mechanical properties of alkali-activated fly ash-slag concrete cured at ambient temperature. Construction and Building Materials 2018;172:476-87.

[32] China Construction Industry Press. Standard for test methods of concrete physical and mechanical properties – GB/T 50081-2019. 2019.

[33] China Construction Industry Press. Test method for basic mechanical properties of fiber reinforced polymer bar – GB/T 30022-2013. 2013.

[34] China Construction Industry Press. Standard for test method of concrete structures – GB/T 50152-2012. 2012.

[35] Maranan G, Manalo A, Benmokrane B, Karunasena W, Mendis P. Shear behavior of geopolymer concrete beams reinforced with glass fiber-reinforced polymer bars. ACI Structural Journal. 2017;114(2).

[36] Ali AH, Mohamed HM, Benmokrane B. Shear behavior of circular concrete members reinforced with GFRP bars and spirals at shear span-to-depth ratios between 1.5 and 3.0. Journal of Composites for Construction. 2016;20(6):04016055.

[37] American Concrete Institute (ACI). Guide for the Design and Construction of Concrete Reinforced with FRP Bars – ACI 440.1 R-06. 2015.

[38] Canadian Standards Association (CSA). Design and construction of building structures with fibre-reinforced polymers – CAN/CSA S802-12. 2012.

[39] Japan Society of Civil Engineers (JSCE). Recommendation for design and construction of concrete structures using continuous fibre reinforcing materials. 1997.

[40] China Construction Industry Press. Technical code for infrastructure application of FRP composites – GB 50608-2010. 2010.

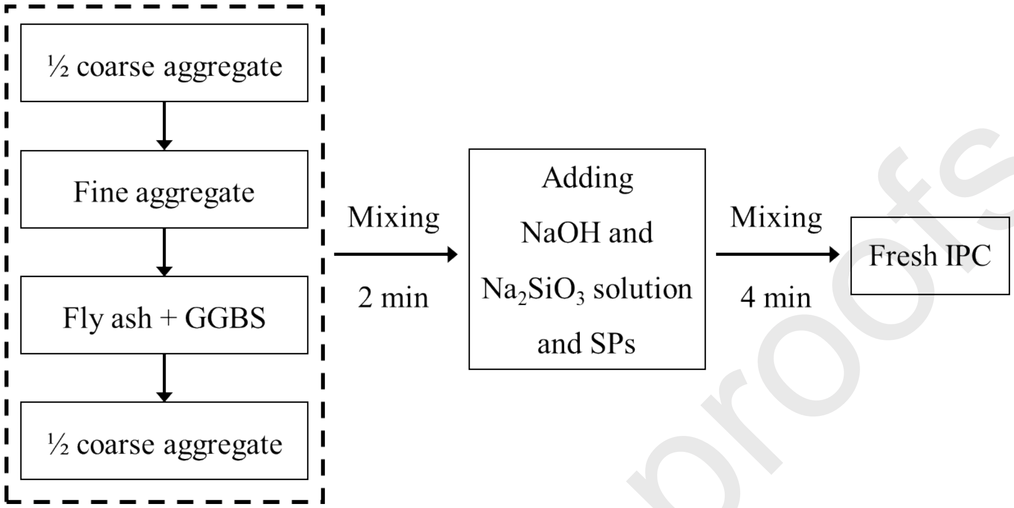

Fig. 1. Mixing procedure for inorganic polymer concrete (IPC).

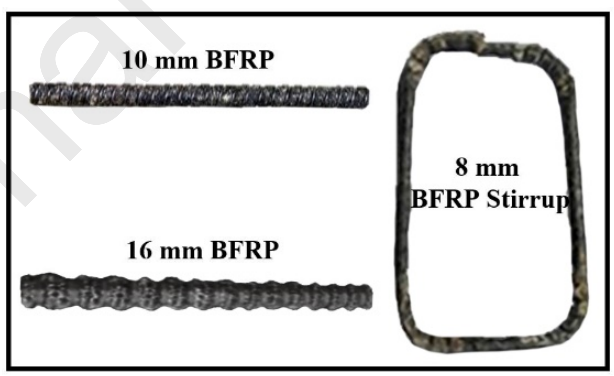

Fig. 2. BFRP longitudinal bars and stirrups.

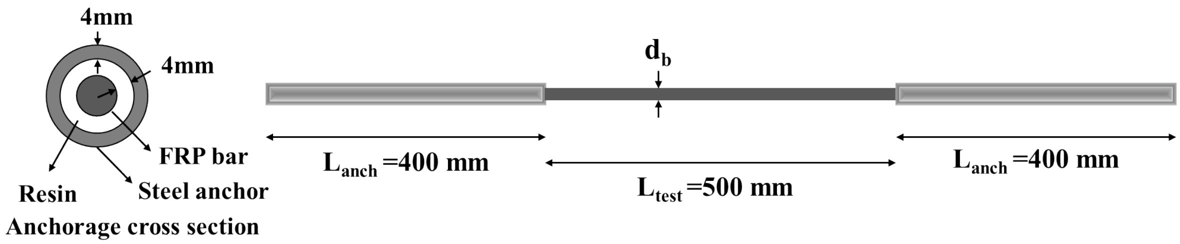

Fig. 3. Dimensions of the tested BFRP bar specimen with steel tubes.

(((

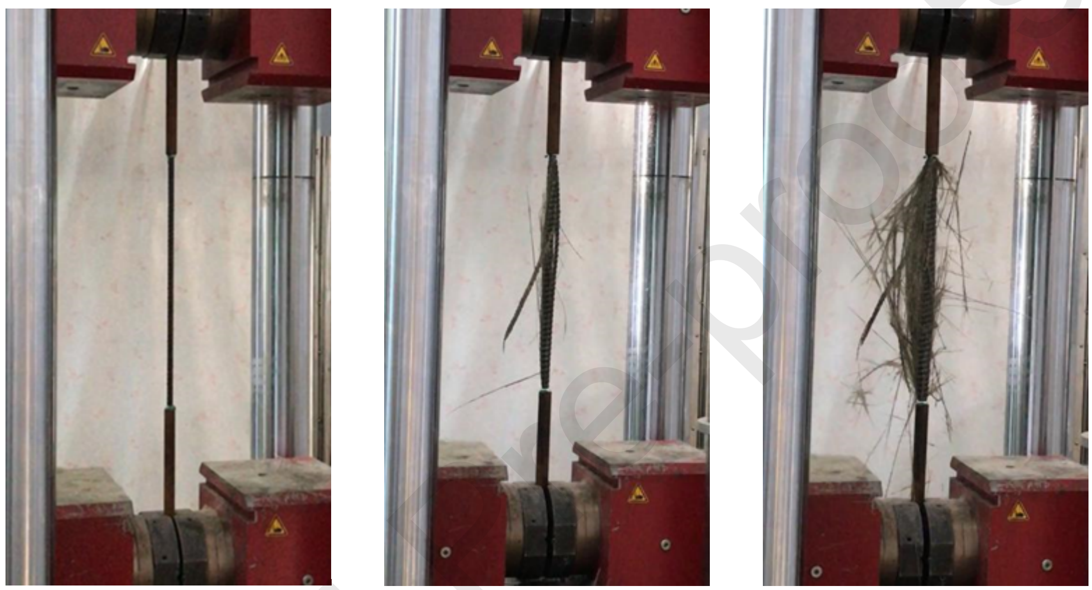

Fig. 4. BFRP bar under uniaxial tension: (a) before, (b) during, and (c) after the test.

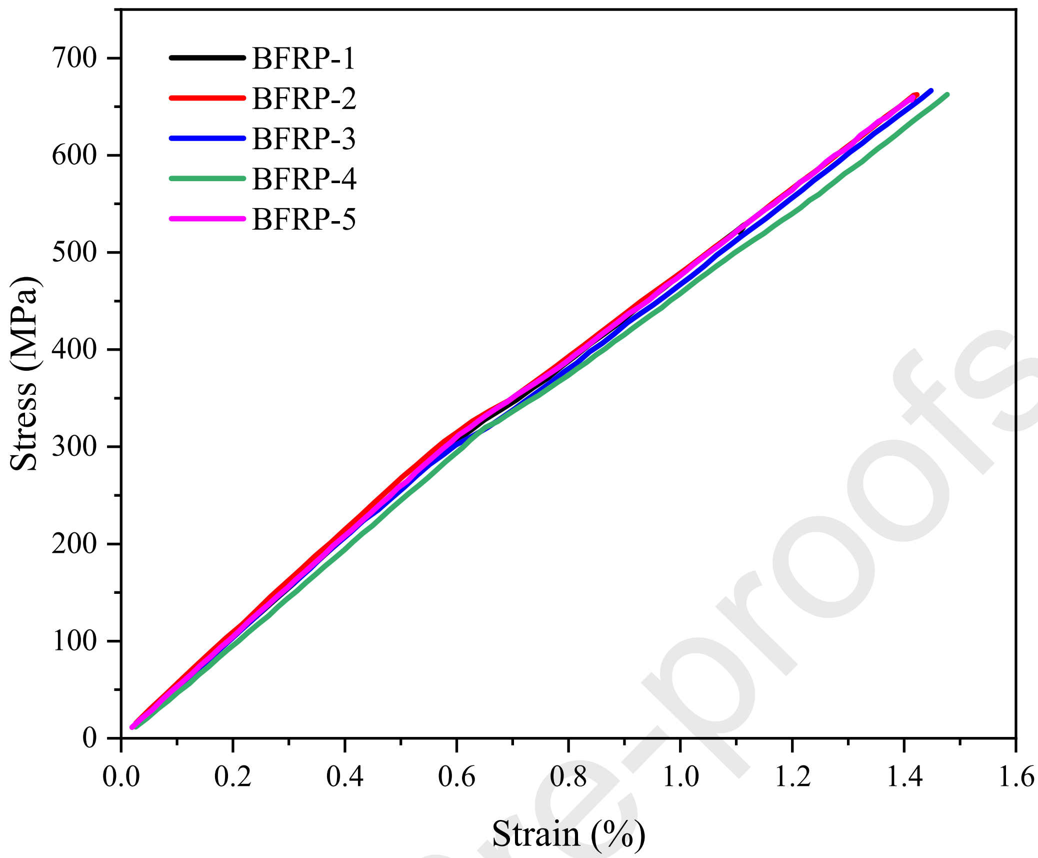

Fig. 5. Stress-strain response of 10-mm BFRP bars under uniaxial tension.

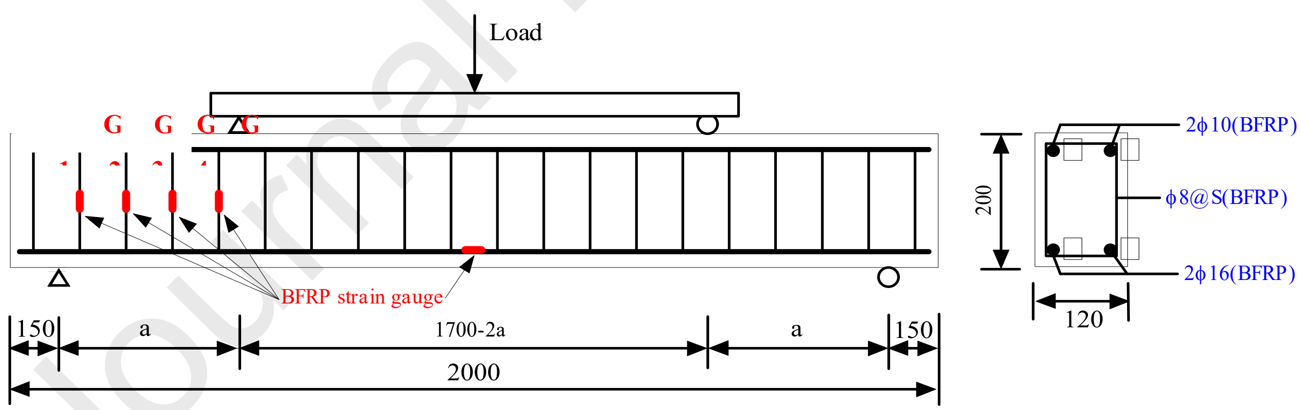

Fig. 6. Four-point bending configuration and details of strain gauges on BFRP reinforcement and concrete (dimensions in mm).

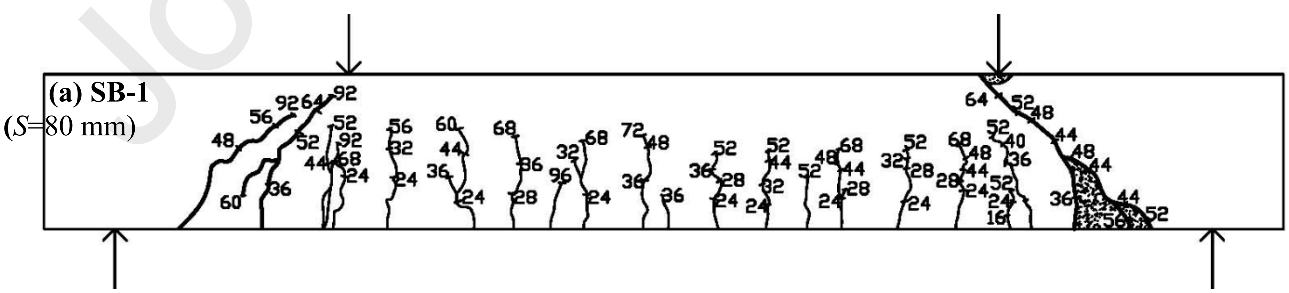

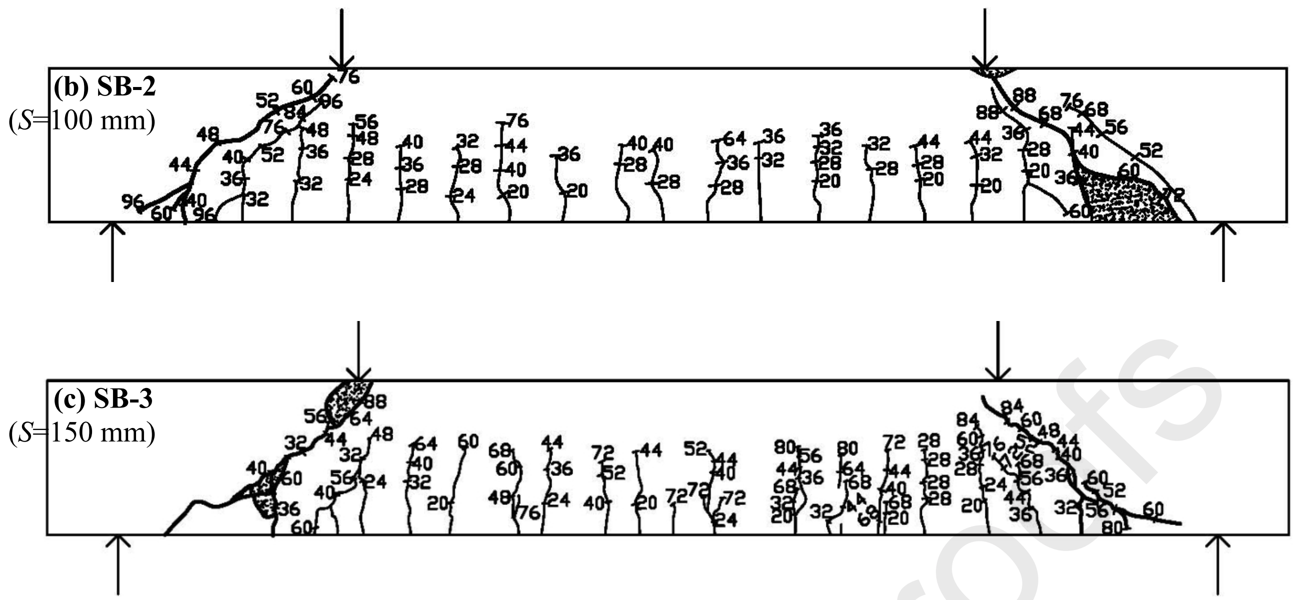

Fig. 7. Crack patterns of BFRP reinforced IPC beams (λ=2.0) with different stirrup spacings (*S* = 80, 100, 150 mm) at failure.

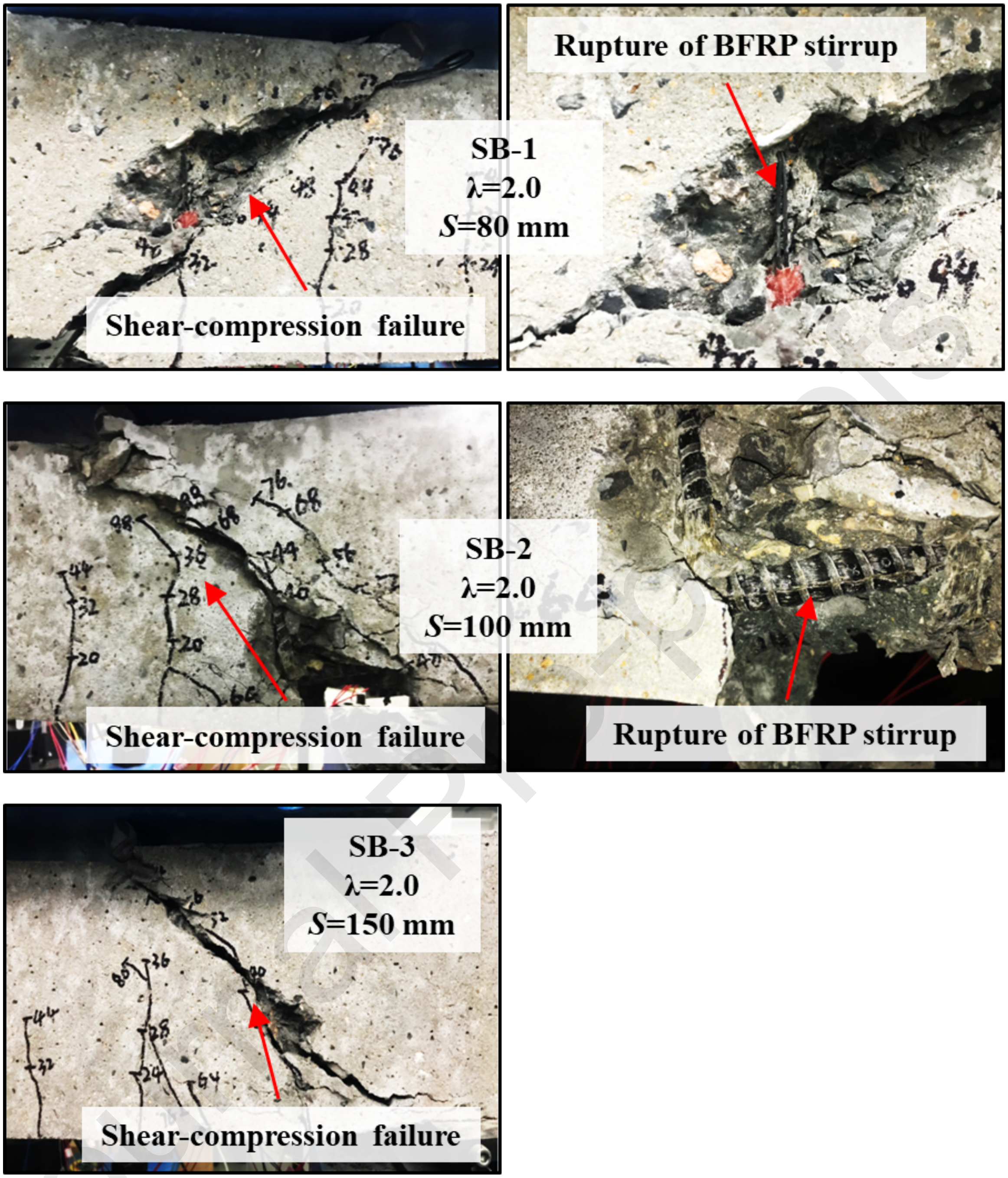

Fig. 8. Failure modes of BFRP reinforced IPC beams (λ=2.0) with different stirrup spacings (S = 80, 100, 150 mm).

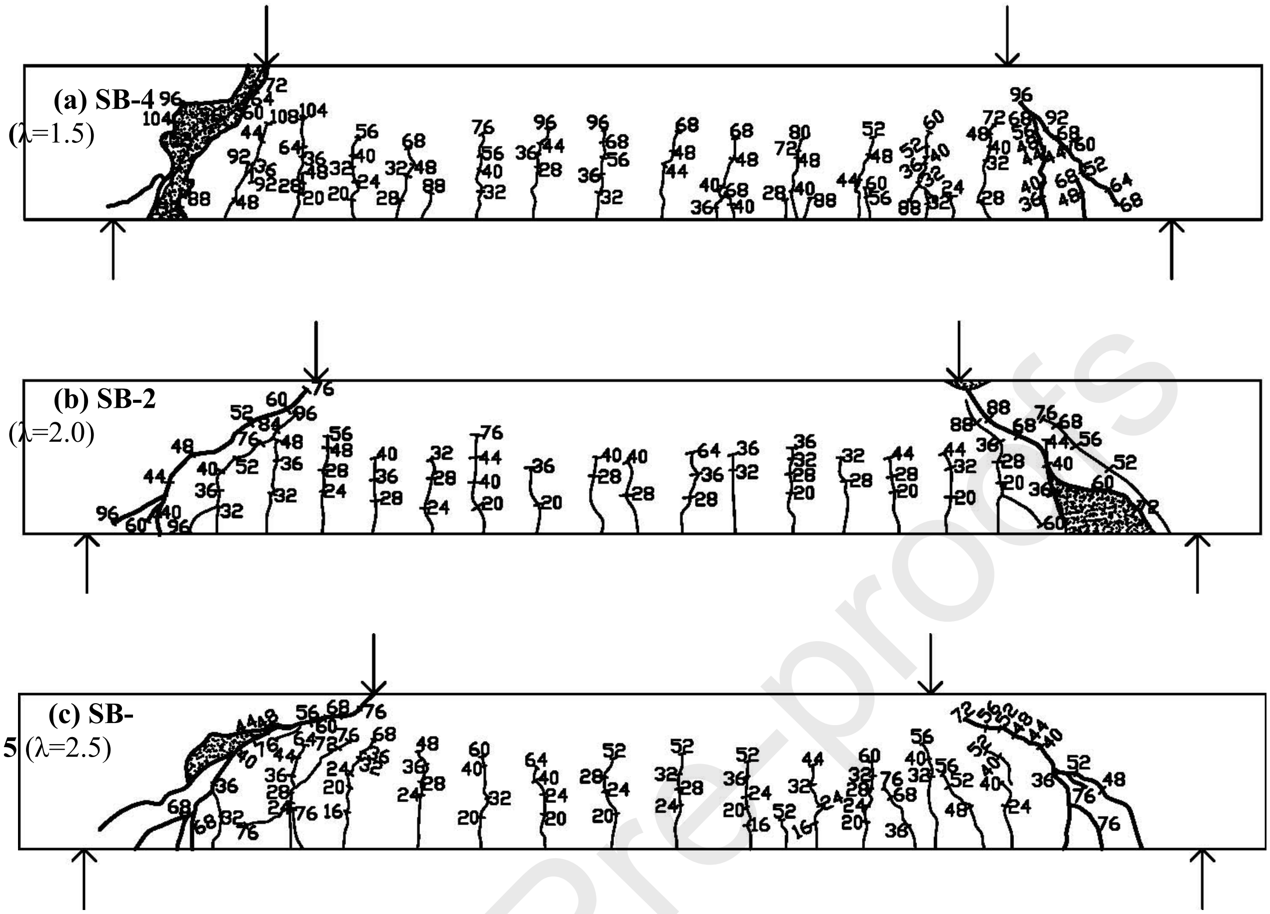

Fig. 9. Crack patterns of BFRP reinforced IPC beams (*S*=100 mm) with different span-to-depth ratios (λ=1.5, 2.0, 2.5) at failure.

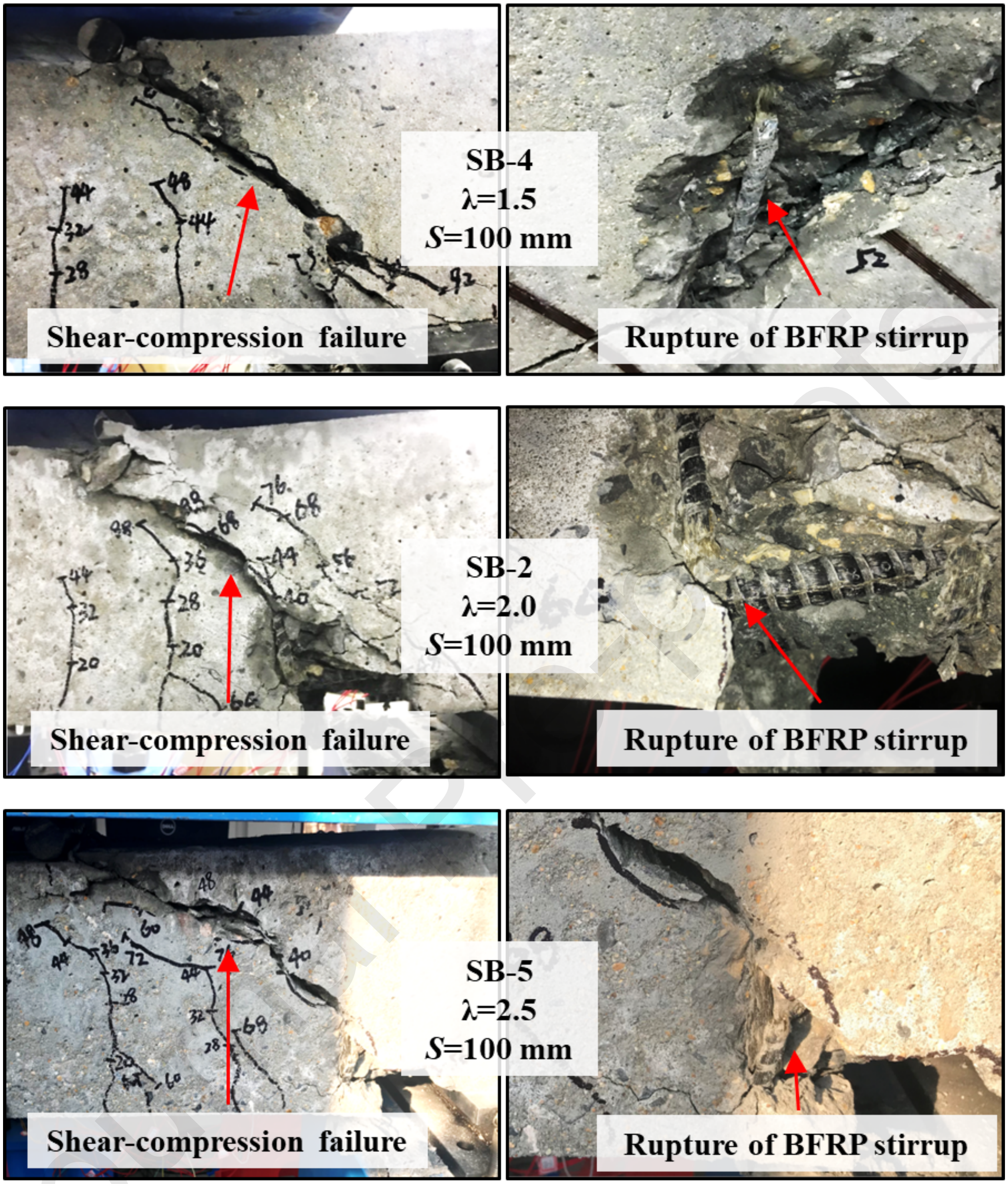

Fig. 10. Failure modes of BFRP reinforced IPC beams (S=100 mm) with different span-to-depth ratios (λ=1.5, 2.0, 2.5).

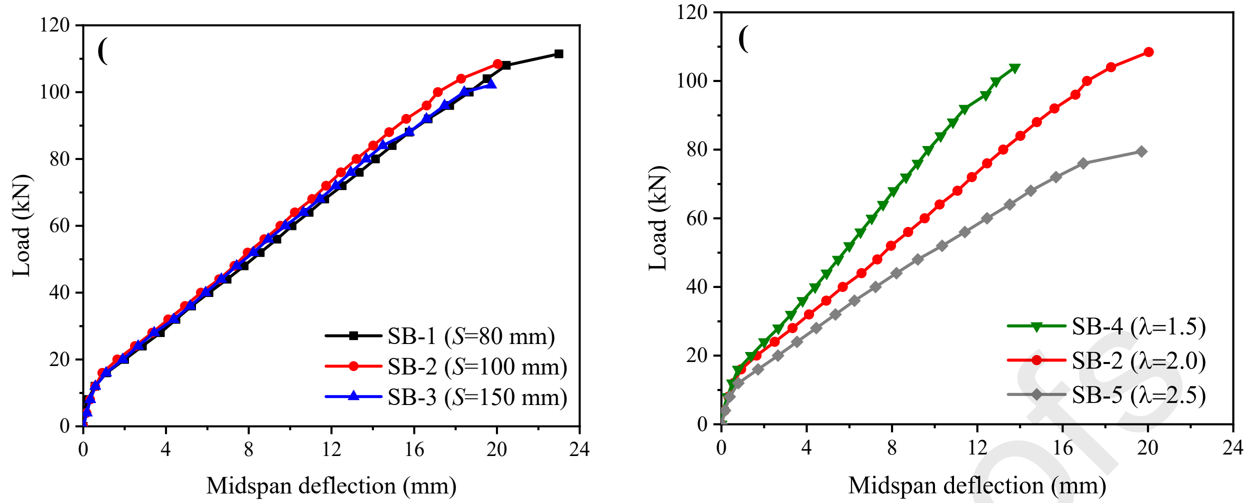

Fig. 11. Load-deflection response of BFRP reinforced IPC beams at midspan regarding the effect of: (a) stirrup spacing (*S*); (b) span-to-depth ratio (λ).

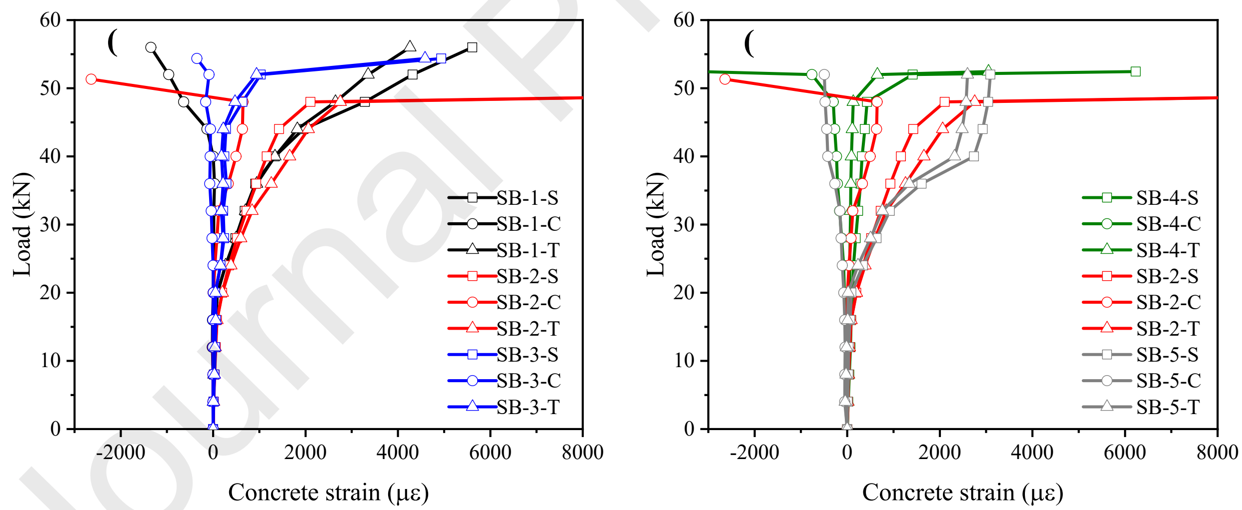

Fig. 12. Load-strain response of concrete at the shear-span area regarding the effect of: (a) stirrup spacing (*S*); (b) span-to-depth ratio (λ).

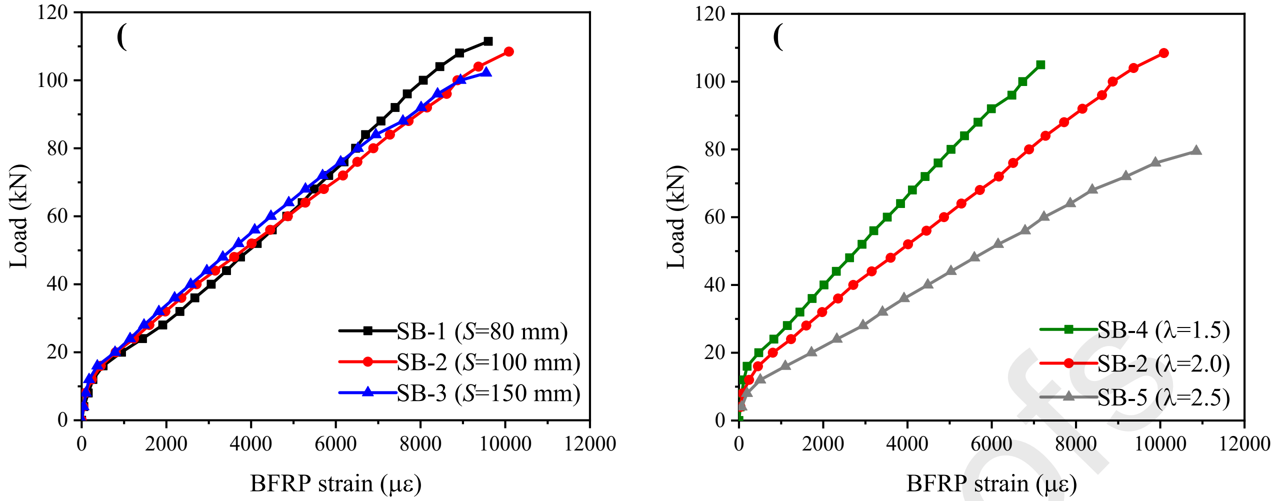

Fig. 13. Load-strain response of longitudinal BFRP bars regarding the effect of: (a) stirrup spacing (S); (b) span-to-depth ratio (λ).

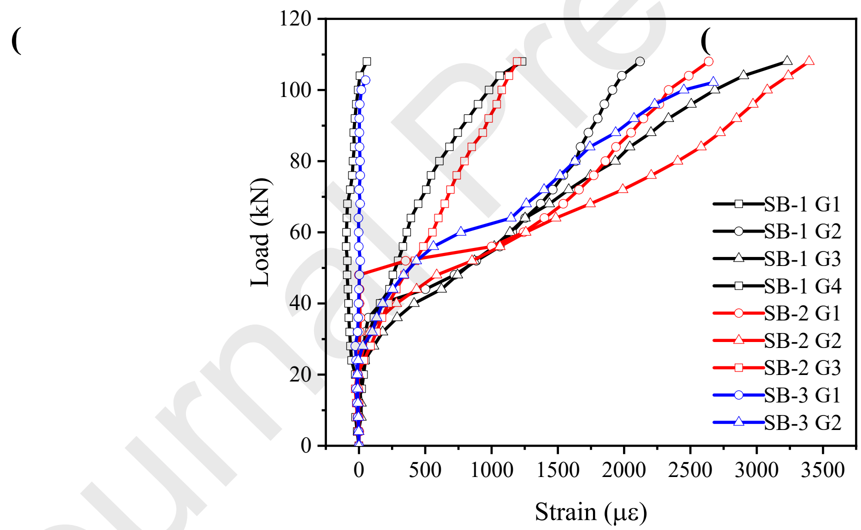

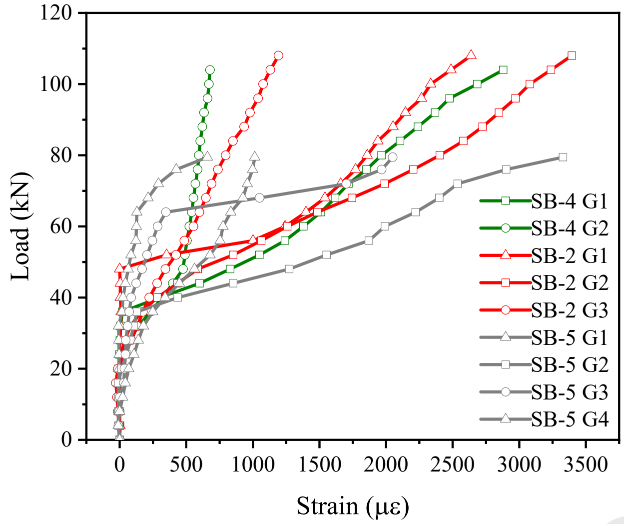

Fig. 14. Load-strain response of BFRP stirrups regarding the effect of: (a) stirrup spacing (*S*); (b) span-to-depth ratio (λ). (G1, G2, G3 and G4 denote the stirrups located from the end of the beams towards the loading point, respectively).

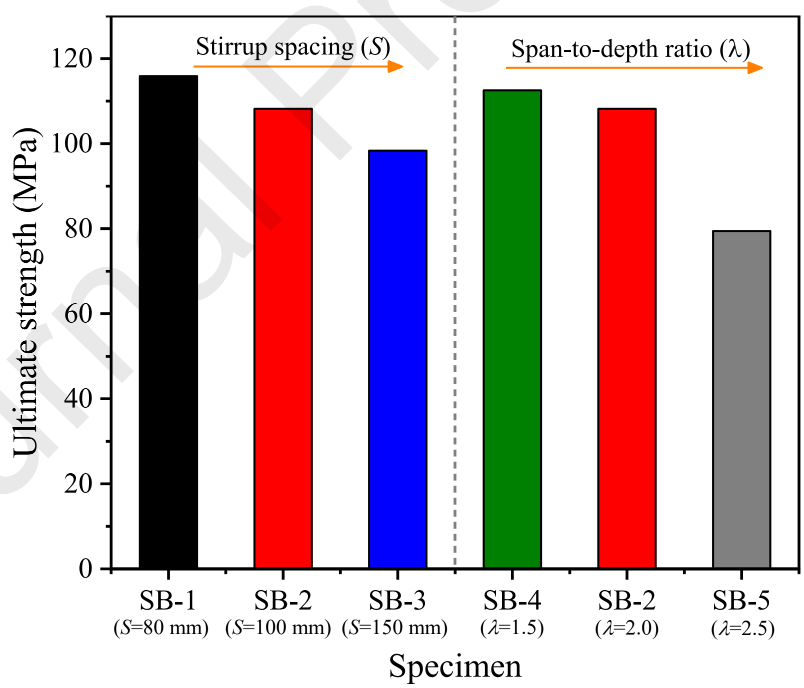

Fig. 15. Effects of stirrup spacing (*S*) and span-to-depth ratio (λ) on ultimate shear capacity of BFRP reinforced IPC beams.

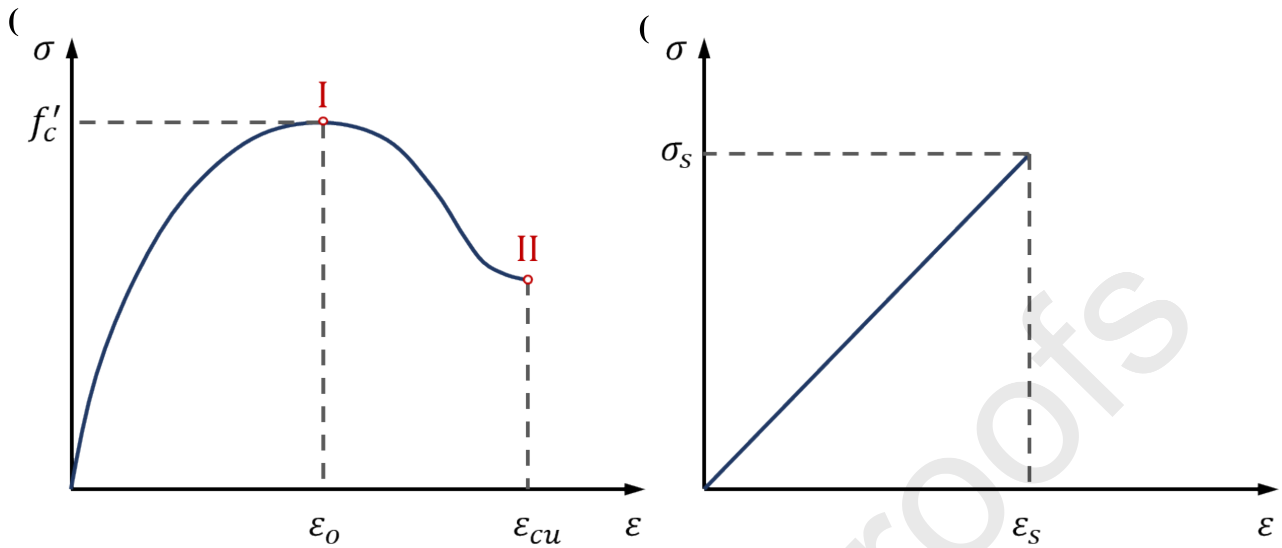

Fig. 16. Schematic diagram of stress-strain relationship of (a) IPC; and (b) BFRP bars.

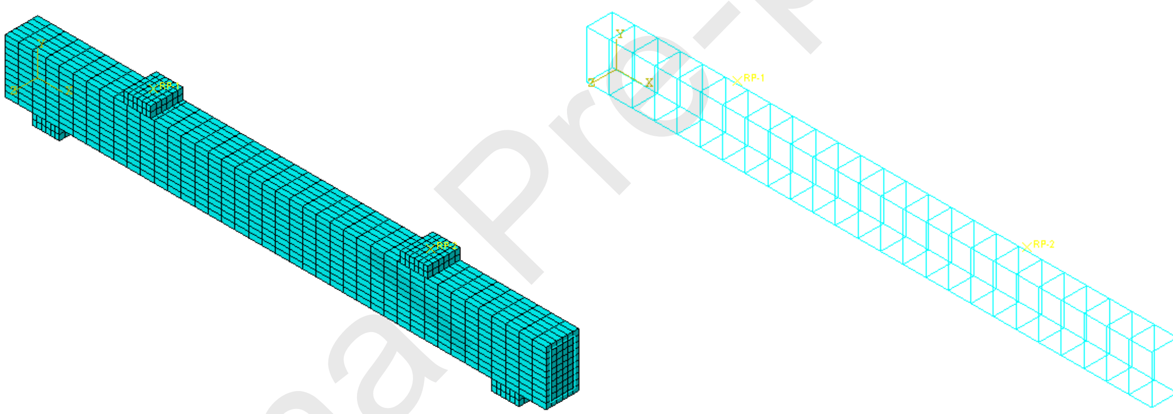

Fig. 17. Finite element model of IPC beam reinforced with BFRP bars and stirrups.

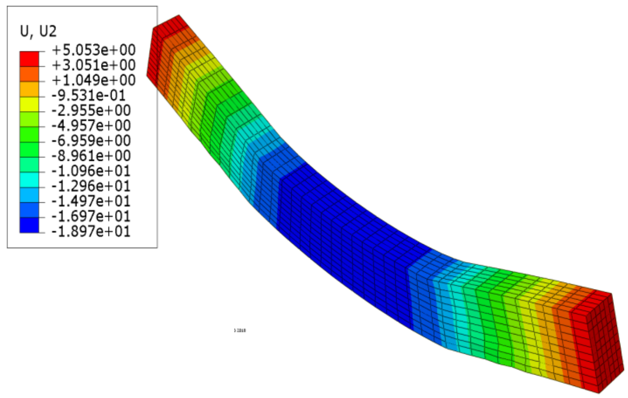

(a) deflection of the beam

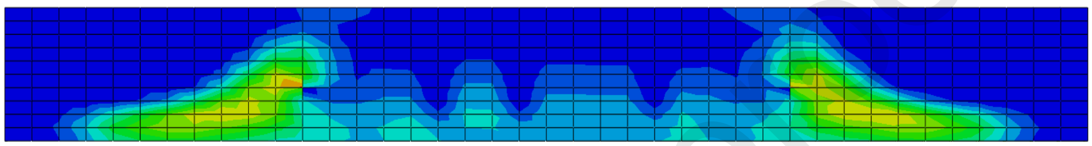

(b) concrete damage

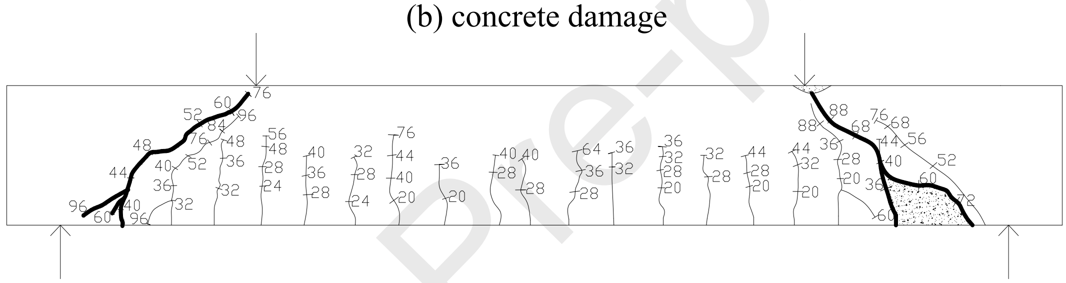

(c) crack pattern of the beam (experiment)

Fig. 18. Finite element simulation results in terms of deflection and cracking of SB-2 compared to experimental data.

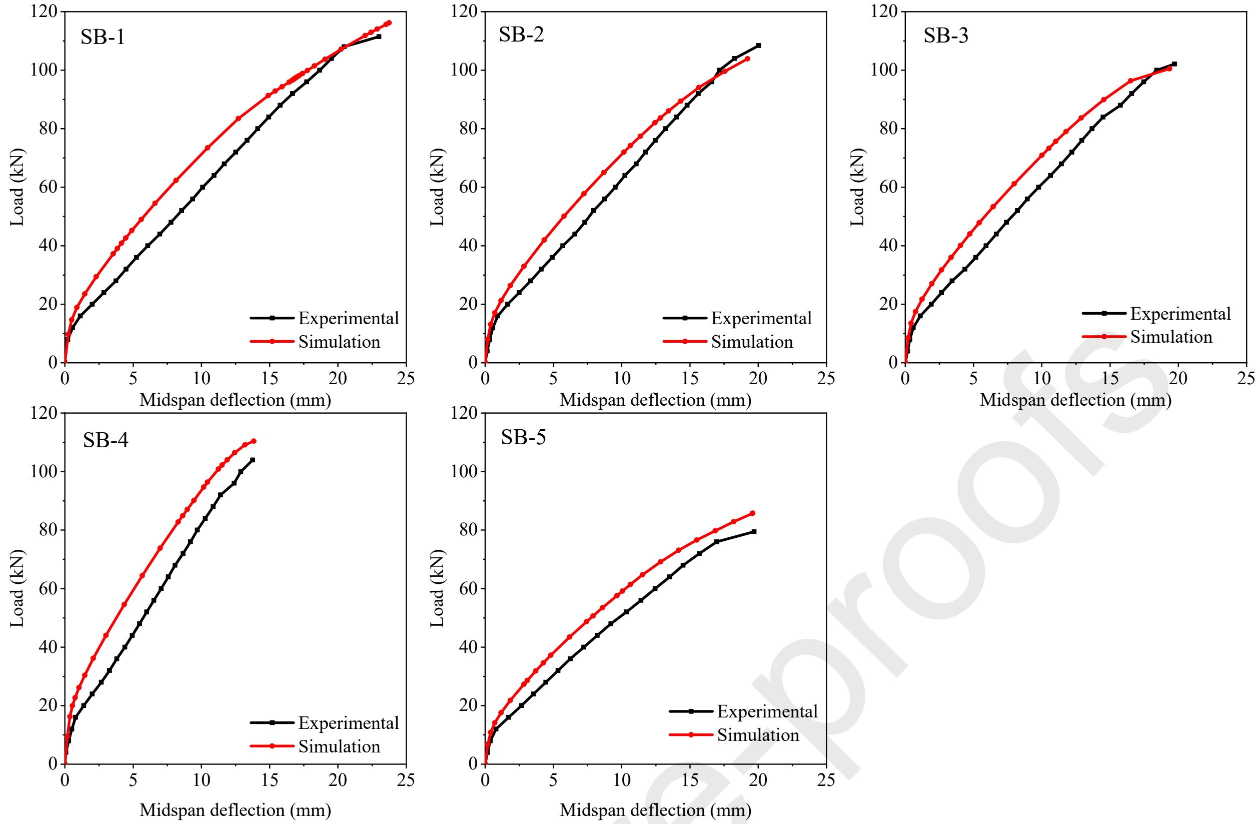

749
750 **Fig. 19.** Comparison of experimental and simulation results in terms of load-deflection curves of
751 the beams at midspan.
752
753
754
755
756

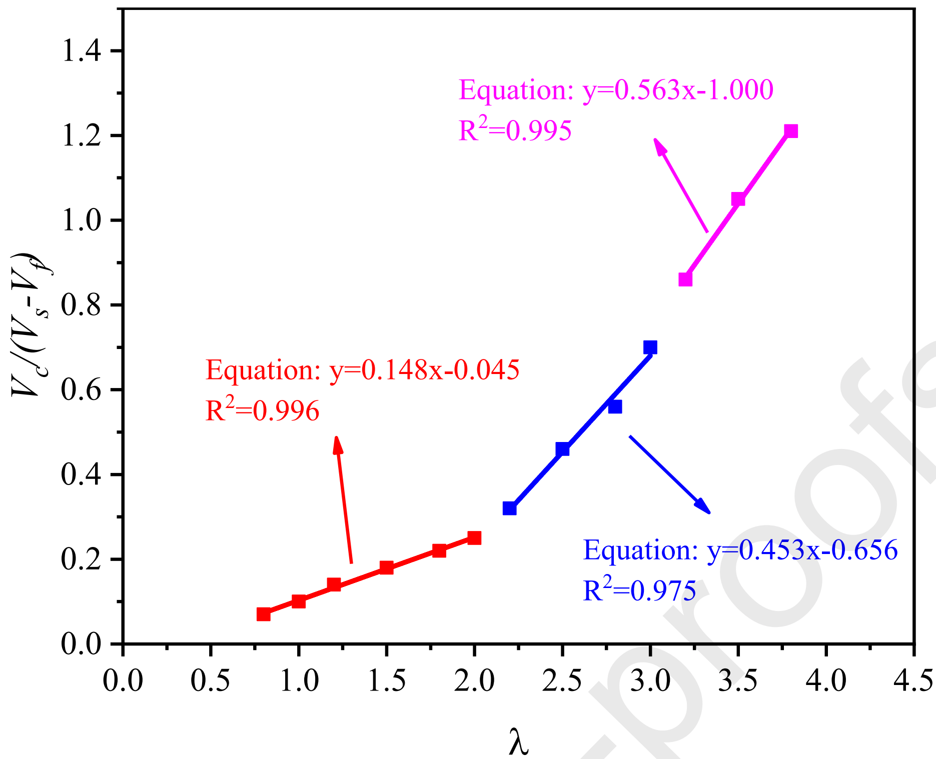

Fig. 20. $V_c/(V_s-V_f)$ against span-to-depth ratio (λ) and the fitting lines.

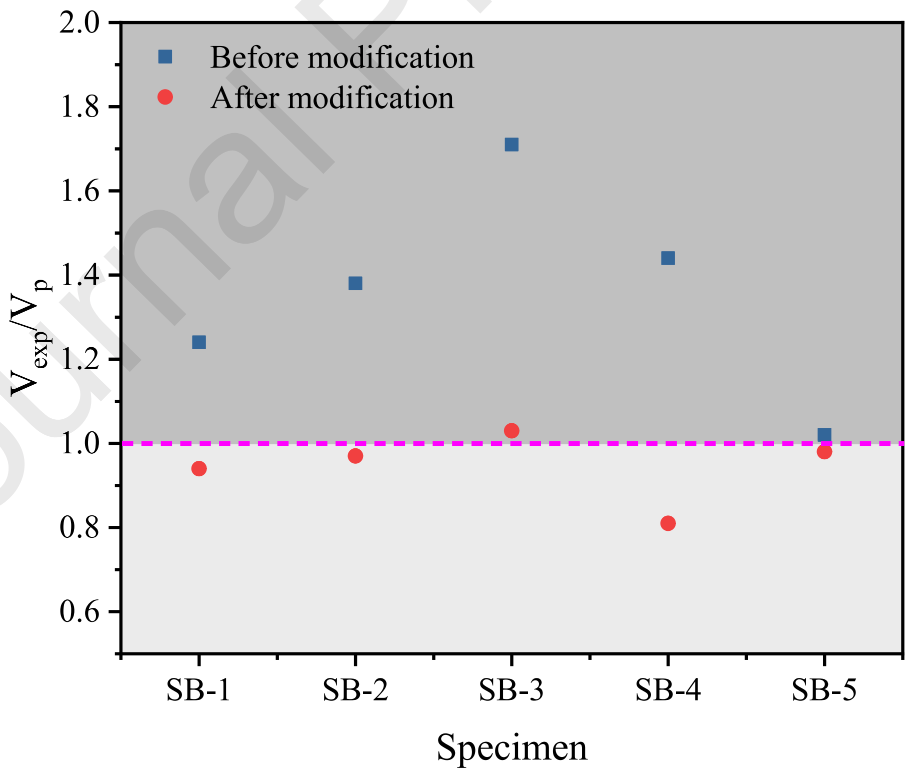

Fig. 21. Comparison between the results of V_{exp}/V_p before and after modification.

Table 1. Chemical compositions (wt%) of FA and GGBS.

Oxide	SiO_2	Al_2O_3	CaO	Fe_2O_3	MgO	SO_3	LOI
FA	51.49	24.36	9.8	5.49	1.2	2.14	2.34
GGBS	35.37	15.74	36.71	0.30	7.62	2.24	2.02

Note: FA (fly ash); GGBS (ground granulated blast-furnace slag); LOI (loss on ignition).

Table 2. Mix proportion of inorganic polymer concrete (IPC) (kg/m^3).

FA	GGBS	SH	SS	SPs	Sand	Crushed stone
300.00	100.00	53.33	106.67	4.00	649.90	1206.96

Note: SS (sodium silicate); SH (sodium hydroxide); SPs (superplasticizers).

Table 3. Mechanical properties of BFRP reinforcement.

Designated diameter (mm)	Minor diameter (mm)	Ultimate tensile strength f_{fu} (MPa)	Elastic modulus E_f (GPa)
8	7.6	1293	50.6
10	8.8	1275	43.4
16	14.08	1212	44.2

Table 4. Details of BFRP reinforced IPC beam specimens.

Beam	Width b (mm)	Depth d (mm)	Top longitudinal bar	Bottom longitudinal bar	Stirrup	a/d
SB-1	120	200	2Φ10	2Φ16	8@80	2.0
SB-2	120	200	2Φ10	2Φ16	8@100	2.0
SB-3	120	200	2Φ10	2Φ16	8@150	2.0
SB-4	120	200	2Φ10	2Φ16	8@100	1.5
SB-5	120	200	2Φ10	2Φ16	8@100	2.5

Table 5. Experimental results of the tested BFRP reinforced IPC beams.

Beam	First crack load (kN)			Ultimate shear load (kN)			Midspan deflection (mm)		
	Specimen #1	Specimen #2	Mean	Specimen #1	Specimen #2	Mean	Specimen #1	Specimen #2	Mean
SB-1	16	20	18	111.44	120.23	115.84	22.65	22.76	22.71
SB-2	20	16	18	108.43	107.97	108.20	20.04	21.61	20.83
SB-3	16	16	18	94.57	102.14	98.35	17.66	19.72	18.69
SB-4	20	20	20	120.13	104.97	112.55	17.69	13.81	15.75
SB-5	16	16	16	-	79.44	79.44	-	19.71	19.71

Table 6. Comparison of predicted (V_p), simulated (V_s) and experimental (V_{exp}) ultimate shear capacities.

Beam	V_{exp} (kN)	ACI 440.1R-06		CSA S806-12		JSCE-97		GB50608-2010		FE simulation	
		V_p (kN)	V_{exp}/V_p	V_p (kN)	V_{exp}/V_p	V_p (kN)	V_{exp}/V_p	V_p (kN)	V_{exp}/V_p	V_s (kN)	V_{exp}/V_s
SB-1	115.84	94.88	1.22	99.32	1.17	36.24	3.20	93.70	1.24	117.82	0.98
SB-2	108.20	79.38	1.36	81.87	1.32	35.12	3.08	78.20	1.38	112.20	0.96
SB-3	98.35	58.7	1.68	58.60	1.68	33.36	2.95	57.52	1.71	98.93	0.99
SB-4	112.55	79.38	1.42	83.83	1.34	35.12	3.20	78.20	1.44	134.94	0.83
SB-5	79.44	79.38	1.00	81.87	0.97	35.12	2.26	78.20	1.02	81.28	0.98
Mean	-	-	1.34	-	1.3	-	2.94	-	1.36	-	0.95
SD	-	-	0.25	-	0.26	-	0.39	-	0.26	-	0.07

Table 7. Comparison of simulated results (V_s) and predictions (V_p) according to GB 50608-2010 [40].

Beam	$\lambda = a/d$	V_s (kN)	V_f (kN)	V_c (kN)	$\frac{1}{\alpha} = \frac{V_c}{V_s - V_f}$
SBS-1	0.8	277.56	46.52	16.16	0.07
SBS-2	1.0	210.47	46.52	16.16	0.10
SBS-3	1.2	158.10	46.52	16.16	0.14
SBS-4	1.5	134.94	46.52	16.16	0.18
SBS-5	1.8	120.42	46.52	16.16	0.22
SBS-6	2.0	112.20	46.52	16.16	0.25
SBS-7	2.2	96.82	46.52	16.16	0.32

SBS-8	2.5	81.28	46.52	16.16	0.46
SBS-9	2.8	75.18	46.52	16.16	0.56
SBS-10	3.0	69.75	46.52	16.16	0.70
SBS-11	3.2	65.39	46.52	16.16	0.86
SBS-12	3.5	61.85	46.52	16.16	1.05
SBS-13	3.8	59.84	46.52	16.16	1.21

The authors declare no conflict of interest.

Xiaochun Fan, Zhengrong Zhou, Wenlin Tu, Mingzhong Zhang

Xiaochun Fan: Conceptualization, Methodology, Funding acquisition, Project administration, Supervision

Zhengrong Zhou: Investigation, Data curation, Visualization, Writing - original draft

Wenlin Tu: Data curation, Visualization, Writing - original draft

Mingzhong Zhang: Conceptualization, Funding acquisition, Project administration, Supervision, Writing - reviewing and editing